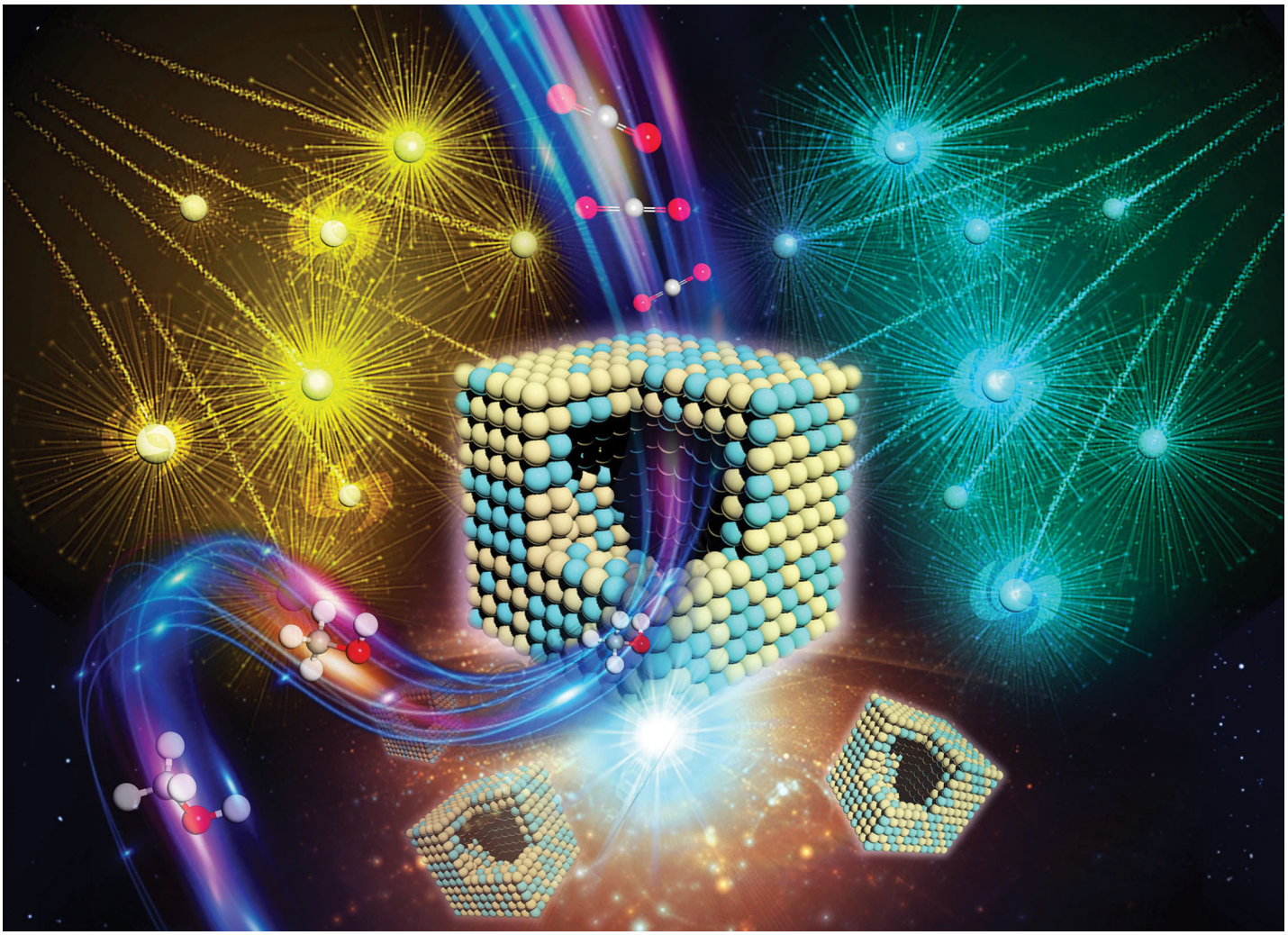

Showcasing research from Professor Xiao-Yu Yang's group, State Key Laboratory of Advanced Technology for Materials Synthesis and Processing, Wuhan University of Technology, Wuhan, China.

PtPd hollow nanocubes with enhanced alloy effect and active facets for efficient methanol oxidation reaction

An alternating-reduction approach by galvanic replacement and co-reduction, which enables incorporation of Pd into Pt shell, is developed to synthesize PtPd hollow nanocubes with highly catalytically-favoured {100} facets and enhanced alloy effect for efficient methanol oxidation reaction.

As featured in:

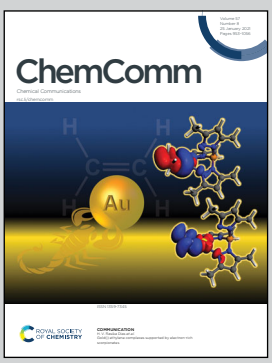

See Jie Ying, Xiao-Yu Yang *et al.*, *Chem. Commun.*, 2021, **57**, 986.

ROYAL SOCIETY OF CHEMISTRY

rsc.li/chemcomm

Registered charity number: 207890

ChemComm

COMMUNICATION

View Article Online
View Journal | View Issue

Cite this: *Chem. Commun.*, 2021, 57, 986

Received 15th October 2020,
Accepted 3rd January 2021

DOI: 10.1039/d0cc06876d

rsc.li/chemcomm

PtPd hollow nanocubes with enhanced alloy effect and active facets for efficient methanol oxidation reaction†

Yu-Xuan Xiao,[a] Jie Ying,*[b] Ge Tian,[a] Xue-Qi Zhang,[a] Christoph Janiak,[c] Kenneth I. Ozoemena[d] and Xiao-Yu Yang*[abe]

We report an alternating-reduction approach by galvanic replacement and co-reduction to enable incorporation of Pd into Pt shell, and the obtained PtPd hollow nanocubes with an enhanced alloy effect and highly active {100} facets show high catalytic activity and superior durability in the methanol oxidation reaction.

Highly cost-effective Pt catalysts should increase the atom utilization efficiency together with controllable nanostructures and facets for high activity and selectivity.[1–3] Hollow nanocubes with {100} facets represent an emerging nanostructure in high-performance Pt design, which exhibit greatly reduced Pt usage and high activity and selectivity of the {100} facets.[4–8] Nanocages with very few atom layers of Pt thus show significant enhancement of electrocatalytic activity and stability.[9–13] It has to be pointed out that this is an elegant idea for the fabrication of catalysts with minimum Pt usage and maximum exposure of highly active {100} facets, in spite of loss of the alloying effect. Bimetallic nanostructured Pt-based metals not only present the physicochemical properties of Pt, but also usually show a superior performance compared with pure Pt counterparts.[14–16] The catalytic activity of bimetallic Pt-based nanoparticles can be greatly enhanced by maximizing the expression of active facets and/or sites toward a specific reaction.[17–19] However, by exploiting Pd nanocubes with exposed {100} facets as a template, it is technically difficult to increase the Pd amount in the Pt shell because a relatively high energy barrier limits the diffusion of Pd.[9] Therefore, an enhancement of the Pd content in PtPd hollow nanocages with dominating {100} factes is rarely reported. Herein, an alternating-reduction approach by galvanic replacement and co-reduction, which we developed, enables incorporation of Pd into a Pt shell. The resultant PtPd hollow nanocubes after etching (denoted as PtPd HNCs-E) possessing an enhanced alloy effect and the highly active {100} facets show catalytic activity and stability in the methanol oxidation reaction (MOR).

Fig. 1 schematically depicts the formation of PtPd HNCs-E. Pd nanocubes with {100} facets as a template were mixed with $H_2PtCl_6{\cdot}6H_2O$ as Pt precursor, KI as selective capping agent, polyvinylpyrrolidone (PVP) as dispersing surfactant, and *N*,*N*-dimethylformamide (DMF) as co-reducing solvent. In our synthetic system, the main reactions for the synthesis of PtPd hollow nanocubes are shown in eqn (1)–(4).

$$[PtCl_6]^{2-} + 6I^- \rightarrow [PtI_6]^{2-} + 6Cl^- \quad (1)$$

$$2Pd + [PtI_6]^{2-} + 2I^- \rightarrow Pt + 2[PdI_4]^{2-} \quad (2)$$

$$[PtI_6]^{2-} \xrightarrow{DMF} Pt + 6I^- \quad (3)$$

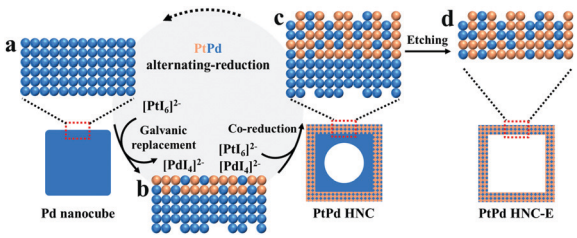

Fig. 1 Scheme for the formation of enhanced alloy effect in PtPd HNCs-E. (a) Pd nanocube and its surface atoms. (b) Growth of Pt atoms by galvanic replacement. (c) Formation of the alloy shell in PtPd HNCs by co-reduction of Pt- and Pd-salts by DMF. (d) Mixed PtPd atoms in PtPd HNCs-E after removal of Pd.

[a] State Key Laboratory of Advanced Technology for Materials Synthesis and Processing & School of Materials Science and Engineering, Wuhan University of Technology, 122 Luoshi Road, Wuhan, 430070, China. E-mail: xyyang@whut.edu.cn
[b] School of Chemical Engineering and Technology, Sun Yat-sen University (SYSU), (Guangdong, Zhuhai) & Southern Marine Science and Engineering Guangdong Laboratory (Zhuhai), Zhuhai, 519000, China. E-mail: yingj5@mail.sysu.edu.cn
[c] Institut für Anorganische Chemie und Strukturchemie, Heinrich-Heine-Universität Düsseldorf, 40204 Düsseldorf, Germany
[d] Molecular Sciences Institute, School of Chemistry, University of the Witwatersrand, Private Bag 3, Johannesburg 2050, South Africa
[e] School of Engineering and Applied Sciences, Harvard University, Cambridge, Massachusetts 02138, USA. E-mail: xyyang@seas.harvard.edu

† Electronic supplementary information (ESI) available: Experimental section, TEM, XPS, CV curves, zeta potential measurements and optical photographs. See DOI: 10.1039/d0cc06876d

$$[PdI_4]^{2-} \xrightarrow{DMF} Pd + 4I^- \quad (4)$$

Despite the selective capping effect, the addition of KI will result in the coordination of I^- and $[PtCl_6]^{2-}$ to form $[PtI_6]^{2-}$ (eqn (1)). The coordination effect can be visualized through the color change from pale yellow to dark color when colorless I^- was added to $[PtCl_6]^{2-}$ (Fig. S1a–c, ESI†), indicating the formation of $[PtI_6]^{2-}$, which could alter the reduction kinetics of Pt(IV). Moreover, the addition of I^- will facilitate the galvanic replacement between Pd and Pt.[20,21] Galvanic replacement would lead to the growth of Pt around the Pd nanocube surface and Pd^{2+} dissolves to form $[PdI_4]^{2-}$ in the presence of KI (Fig. 1a and b, eqn (2)), as can be visualized through the color change from brown to dark color (Fig. S1d and e, ESI†). Then, a co-reduction of Pt(IV) and Pd(II) by DMF would occur (eqn (3) and (4)). Such an alternating-reduction by galvanic replacement and co-reduction will incorporate Pd atoms into the Pt shell (Fig. 1c). The dissolution of the Pd core and deposition of Pd into a growing Pt shell will be repeated several times, resulting in the hollow structure of the PtPd nanocubes (denoted as PtPd HNCs). Finally, the unstable Pd template in the interior of the PtPd HNCs would be removed by acid etching, resulting in PtPd HNCs-E with highly active {100} facets (Fig. 1d). To gain more insight into the formation of the PtPd alloy shell, zeta potentials were measured to characterize the surface charges of nanometals. The value of the zeta potential was changed during the synthesis process of PtPd-HNCs, starting from −8.42 mV (Pd nanocubes), to −23.2 mV (10 min), −12.4 mV (30 min), −13.6 mV (60 min), −14.2 mV (90 min) and −14.0 mV (120 min) (Fig. S2, ESI†). Compared to the zeta potential of Pt nanocrystals (−33.6 mV), the increased value at 10 min indicates the formation of surface Pt, and the decreased value at 30 min indicates the formation of a PtPd alloy. The zeta potential value was kept almost unchanged from 60 to 120 min, which illustrates a nearly unchanged structure and stable state of the PtPd shell.

The nanostructure of PtPd HNCs-E can be visualized by transmission electron microscopy (TEM) images in Fig. 2a and b, exhibiting an obviously conformal and hollow structure with the average diameter of 24 nm. Considering the average diameter of 20 nm for the original Pd nanocubes (Fig. S3a and b, ESI†), the thickness of the shell can be calculated as 4 nm. Two selected regions in Fig. 2b are enlarged as shown in Fig. 2c and e, and their corresponding fast Fourier transform (FFT) results are shown in Fig. 2d and f, respectively. PtPd HNCs-E exhibited a lattice spacing of 0.195 nm, which is between 0.194 and 0.196 nm, corresponding to the {100} interplanar distance of face-centered cubic (fcc) palladium and platinum, respectively. Compared to the spacing of 0.194 nm of Pd nanocubes (Fig. S3c, ESI†) and 0.195 nm of PtPd HNCs (Fig. S4, ESI†), the PtPd HNCs-E showed an alloy structure of PtPd and unchanged shell structure from PtPd HNCs. Moreover, two sets of spots in FFT can be identified as the reflections of the PtPd (200) and (400) planes. All these results suggest that the PtPd HNCs-E are dominantly enclosed by {100} facets. Fig. 2g and h show the

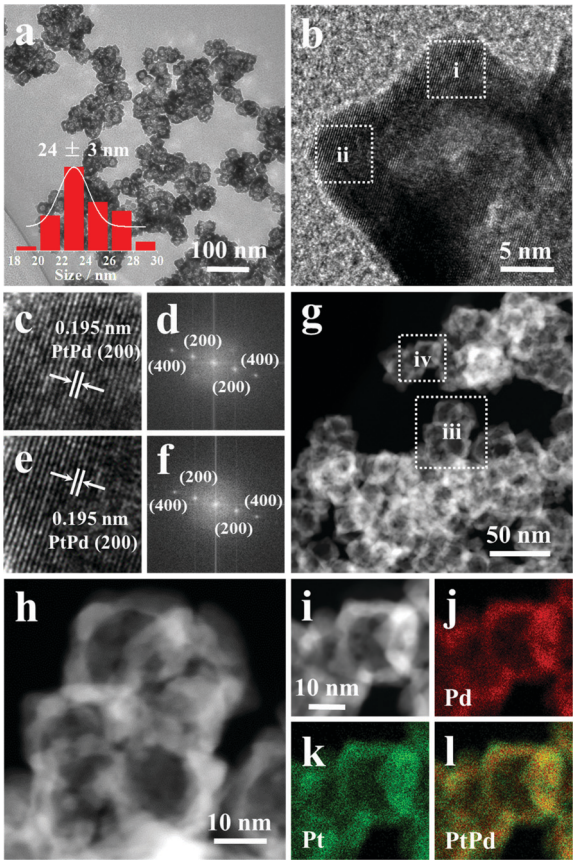

Fig. 2 (a) Low and (b) high magnification TEM images of PtPd HNCs-E. The inset of a is the particle size distribution of PtPd HNCs-E. (c) Lattice fringes and (d) corresponding FFT results of region i in b. (e) Lattice fringes and (f) corresponding FFT results of region ii in b. (g) Low magnification HAADF-STEM image of PtPd HNCs-E. Magnifying images of (h) region iii and (i) region iv in g. EDX mapping of region iv showing the signal of (j) Pd, (k) Pt, and (l) overlaid Pt and Pd.

high-angle annular dark-field scanning TEM (HAADF-STEM) images with different magnifications. Under dark field, the hollow structure can be seen more clearly. Fig. 2i–l show the elemental mapping of PtPd HNCs-E measured by HAADF-STEM energy-dispersive X-ray spectroscopy (HAADF-STEM-EDX). As can be seen, Pt and Pd elements are homogeneously dispersed throughout the nanoparticles except for very small amounts of Pt elements dispersed in the outer surface, indicating the high alloying degree with a Pt-rich surface in PtPd HNCs-E. According to the results of inductively coupled plasma-atomic emission spectrometry (ICP-AES), the atomic ratio of Pt : Pd was 2 : 1 in the PtPd HNCs-E. Notably, the Pd content in the PtPd HNCs-E is much higher than those reported for etched PtPd nanocages.[9,10,22,23] The remaining Pd content indicates a stable alloy structure of PtPd HNCs-E which can resist the further etching of HNO_3 even lasting for five days.

To investigate the crystal structure changes among Pd nanocubes, PtPd HNCs, and PtPd HNCs-E, X-ray diffraction (XRD) measurements were conducted. As shown in Fig. 3a, five peaks around 40°, 46°, 68°, 82°, and 87° can be readily indexed to the (111), (200), (220), (311) and (222) reflections of fcc Pt

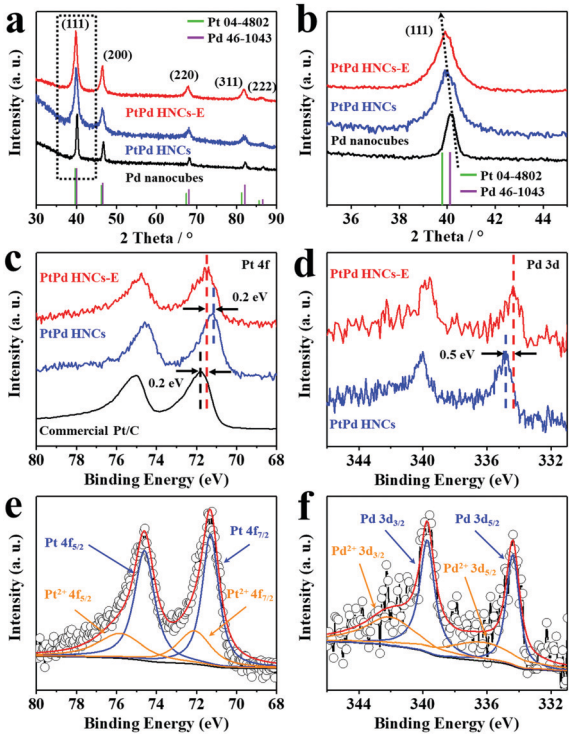

Fig. 3 (a) XRD patterns of Pd nanocubes, PtPd HNCs, and PtPd HNCs-E. (b) Magnified pattern of the (111) peak in a. (c) XPS spectra showing the binding energy of Pt 4f for PtPd HNCs-E, PtPd HNCs and commercial Pt/C. (d) XPS spectra showing the binding energy of Pd 3d for PtPd HNCs-E and PtPd HNCs. Peak fitting results of the (e) Pt 4f and (f) Pd 3d signal of PtPd HNCs-E.

(ICDD no. 04-4802) and Pd (ICDD no. 46-1043), which are in agreement with those of the previous reports.[24,25] Fig. 3b shows the magnified patterns of the (111) peaks. As can be seen, the position of the peaks is shifted to lower angle from Pd nanocubes to PtPd HNCs-E, which indicates the gradual increase of Pt content after Pt coating and Pd removal. X-ray photoelectron spectroscopy (XPS) spectra were used to study the chemical states of Pt and Pd in PtPd HNCs and PtPd HNCs-E. Commercial Pt/C was also tested for comparison. As shown in Fig. 3c, compared to commercial Pt/C, the binding energies of Pt 4f for both PtPd HNCs-E and PtPd HNCs exhibit a downshift. This result indicates a strong alloy effect and a downshifted d-band center exists in PtPd HNCs-E and PtPd HNCs,[26,27] which originates from the electron transfer from Pd to Pt owing to the different values of electronegativity for Pd (2.20) and Pt (2.28). Moreover, compared to PtPd HNCs, the binding energies of Pt 4f for PtPd HNCs-E is shifted 0.2 eV to a higher value, which is owing to the removal of Pd in the cores of PtPd HNCs. In addition, PtPd HNCs-E show a 0.5 eV downshift compared to PtPd HNCs with respect to the Pd 3d binding energies (Fig. 3d). These results demonstrate the removal of Pd from PtPd HNCs and the increase of Pt content in PtPd HNCs-E. Fig. 3e and f show the Pt 4f and Pd 3d peak fitting results of PtPd HNCs-E. The results clearly demonstrate that there is mainly Pt^0 and Pd^0 with partial Pt^{2+} and Pd^{2+} on the surface of PtPd HNCs-E. Compared to PtPd HNCs (Fig. S5, ESI†), the relative intensity of Pt^{2+} is changed from 23% to 33% and Pd^{2+} from 29% to 47% in PtPd HNCs-E owing to the surface oxidation after nitric acid treatment.

The electrocatalytic activities of PtPd HNCs-E for the MOR were investigated in comparison to PtPd HNCs and commercial Pt/C under the same conditions. The mechanism of the MOR on the PtPd alloy is depicted in Fig. S6, ESI.† The electrochemically active surface areas (ECSAs), which were calculated based on charges involved in the adsorption of hydrogen in the cyclic voltammograms (CVs) recorded in 0.1 M KOH (Fig. 4a), were 25.5, 23.5, and 51.7 $m^2\ g_{metal}^{-1}$ for PtPd HNCs-E, PtPd HNCs, and commercial Pt/C, respectively. Fig. 4b shows the CV curves of these electrocatalysts for the MOR. The onset potential of PtPd HNCs-E is much lower than that of both PtPd HNCs and commercial Pt/C, indicating that the oxidation of methanol is much easier to be triggered on the surface of PtPd HNCs-E.[28,29] The mass activities and specific activities for these three catalysts are summarized in Fig. 4c and Table S1, ESI.† PtPd HNCs-E exhibit a mass activity of 1.7 mA μg_{metal}^{-1}, which is 1.9 and 3.5 times that of PtPd HNCs (0.89 mA μg_{metal}^{-1}) and commercial Pt/C catalysts (0.49 mA μg_{metal}^{-1}), respectively. In addition, PtPd HNCs-E exhibit the highest specific value of 6.7 mA cm^{-2}, which is 1.8 and 7.1 times that of PtPd HNCs (3.8 mA cm^{-2}) and commercial Pt/C catalysts (0.95 mA cm^{-2}), respectively. Notably, the catalytic activities of PtPd HNCs-E towards the MOR are also superior to that of other previously reported Pt-based catalysts (Table S2, ESI†). Moreover, PtPd HNCs-E also exhibit the best MOR activities performed in 0.5 M

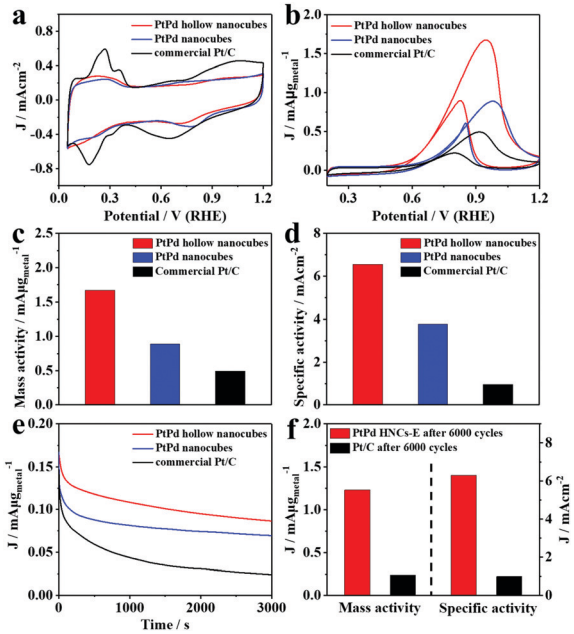

Fig. 4 CV curves of PtPd HNCs-E, PtPd HNCs, and commercial Pt/C recorded in (a) 0.1 M KOH and (b) 0.1 M KOH + 1 M CH_3OH. (c) Mass activity and (d) specific activity of PtPd HNCs, PtPd HNCs-E, and commercial Pt/C. (e) Chronoamperometry measurements of PtPd HNCs-E, PtPd HNCs, and commercial Pt/C in 0.1 M KOH + 1 M CH_3OH at 0.8V (RHE). (f) Mass activity and specific activity of PtPd HNCs-E and commercial Pt/C after 6000 cycles of ADTs.

and 2 M methanol (Fig. S7, ESI†). The improved electrocatalytic properties of PtPd HNCs-E can be attributed to the catalytically preferential {100} facets of hollow cubic structures and the downshift of the d-band center of the Pt electronic structure induced by an electronic interaction between the PtPd alloy. Furthermore, CO stripping measurement results showed that PtPd HNCs-E exhibited the best CO tolerance ability (Fig. S8, ESI†).

Chronoamperometric curves were recorded to probe the stability of the catalysts (Fig. 4e). PtPd HNCs-E show a higher specific current density and slower current decay than PtPd HNCs and commercial Pt/C during the whole test process, demonstrating the highest electrocatalytic stability of PtPd HNCs-E for the MOR. Furthermore, the durability of PtPd HNCs-E and commercial Pt/C was studied by performing accelerated durability tests (ADTs) at room temperature in 0.1 M KOH. After 6000 cycles of ADT, a slight drop of current density can be found for PtPd HNCs-E with increasing CV cycle numbers (Fig. S9a, ESI†), while a conspicuous drop for commercial Pt/C is seen (Fig. S9b, ESI†). After 2000, 4000, and 6000 cycles, the specific ECSA of PtPd HNCs-E only dropped by 13%, 18%, and 23%, whereas the specific ECSA of the commercial Pt/C catalyst sharply decreased by 28%, 41%, and 54% (Fig. S10 and Table S3, ESI†). Moreover, the characterization after 6000 cycles of the ADTs indicates the higher MOR durability and stable morphology of PtPd HNCs-E compared to commercial Pt/C (Fig. 4f and Fig. S11–13, ESI†). These results demonstrate that in addition to high MOR activity and CO tolerance, PtPd HNCs-E also exhibit superior electrochemical durability.

In summary, we have presented an effective strategy to synthesize PtPd HNCs-E with exposed {100} active facets and optimized alloy structures. PtPd HNCs-E exhibit 3.5 times the mass activity and a remarkable 7.1 times of the specific activity, as well as much higher CO tolerance and durability than a commercial Pt/C catalyst in the MOR. The enhanced electrocatalytic performance of PtPd HNCs-E could be ascribed to the cubic morphology with catalytically-favoured {100} facets, to he hollow structure with more exposed Pt active sites, and to the synergetic effects from the enhanced alloy effect of PtPd bimetals. This work displays new possibilities for designing novel nanomaterials with high activity and superior stability towards methanol electrooxidation or other practical applications.

This work was supported by a joint National Natural Science Foundation of China-Deutsche Forschungsgemein-schaft (NSFC-DFG) project (NSFC grant 51861135313, DFG JA466/39-1), Sino-German Center COVID-19 Related Bilateral Collaborative project (C-0046), JPSTDP (20180101208JC), FRFCU (19lgz d16, 20lgpy77), ISTCP (2015DFE52870), Guangdong Basic and Applied Basic Research Foundation (2019A1515110436), Guangdong Province International Scientific and Technological Cooperation Projects (2020A0505100036), and South Africa's National Research Foundation (No. 113638).

Conflicts of interest

There are no conflicts to declare.

References

1 C. Chen, Y. Kang, Z. Huo, Z. Zhu, W. Huang, H. L. Xin, J. D. Snyder, D. Li, J. A. Herron, M. Mavrikakis, M. Chi, K. L. More, Y. Li, N. M. Markovic, G. A. Somorjai, P. Yang and V. R. Stamenkovic, *Science*, 2014, **343**, 1339–1343.
2 X. Zhao, S. Chen, Z. Fang, J. Ding, W. Sang, Y. Wang, J. Zhao, Z. Peng and J. Zeng, *J. Am. Chem. Soc.*, 2015, **137**, 2804–2807.
3 K. Deng, Y. Xu, D. Yang, X. Qian, Z. Dai, Z. Wang, X. Li, L. Wang and H. Wang, *J. Mater. Chem. A*, 2019, **7**, 9791–9797.
4 S.-C. Lin, C.-S. Hsu, S.-Y. Chiu, T.-Y. Liao and H. M. Chen, *J. Am. Chem. Soc.*, 2017, **139**, 2224–2233.
5 Y. Ai, Z. Hu, L. Liu, J. Zhou, Y. Long, J. Li, M. Ding, H.-B. Sun and Q. Liang, *Adv. Sci.*, 2019, **6**, 1802132.
6 X. Yang, L. T. Roling, M. Vara, A. O. Elnabawy, M. Zhao, Z. D. Hood, S. Bao, M. Mavrikakis and Y. Xia, *Nano Lett.*, 2016, **16**, 6644–6649.
7 J.-Y. Wang, X. Mu, Y. Li, F. Xu, W. Long, J. Yang, P. Bian, J. Chen, L. Ouyang, H. Liu, Y. Jing, J. Wang, L. Liu, H. Dai, Y. Sun, C. Liu and X.-D. Zhang, *Small*, 2018, **14**, 1703736.
8 Y. Wang, L. Zhang, C. Hu, S. Yu, P. Yang, D. Cheng, Z.-J. Zhao and J. Gong, *Nano Res.*, 2019, **12**, 2268–2274.
9 L. Zhang, L. T. Roling, X. Wang, M. Vara, M. Chi, J. Liu, S.-I. Choi, J. Park, J. A. Herron, Z. Xie, M. Mavrikakis and Y. Xia, *Science*, 2015, **349**, 412–416.
10 D. S. He, D. He, J. Wang, Y. Lin, P. Yin, X. Hong, Y. Wu and Y. Li, *J. Am. Chem. Soc.*, 2016, **138**, 1494–1497.
11 J. Zhu, M. Xie, Z. Chen, Z. Lyu, M. Chi, W. Jin and Y. Xia, *Adv. Energy Mater.*, 2020, **10**, 1904114.
12 X. Sun, X. Yang, Y. Zhang, Y. Ding, D. Su and D. Qin, *Nanoscale*, 2017, **9**, 15107–15114.
13 X. Wang, L. Figueroa-Cosme, X. Yang, M. Luo, J. Liu, Z. Xie and Y. Xia, *Nano Lett.*, 2016, **16**, 1467–1471.
14 L. Bu, N. Zhang, S. Guo, X. Zhang, J. Li, J. Yao, T. Wu, G. Lu, J.-Y. Ma, D. Su and X. Huang, *Science*, 2016, **354**, 1410–1414.
15 J. Ying, X.-Y. Yang, Z.-Y. Hu, S.-C. Mu, C. Janiak, W. Geng, M. Pan, X. Ke, G. Van Tendeloo and B.-L. Su, *Nano Energy*, 2014, **8**, 214–222.
16 J. Ying, G. Jiang, Z. P. Cano, Z. Ma and Z. Chen, *Appl. Catal., B*, 2018, **236**, 359–367.
17 X. Huang, Z. Zhao, L. Cao, Y. Chen, E. Zhu, Z. Lin, M. Li, A. Yan, A. Zettl, Y. M. Wang, X. Duan, T. Mueller and Y. Huang, *Science*, 2015, **348**, 1230–1234.
18 Z. Niu, N. Becknell, Y. Yu, D. Kim, C. Chen, N. Kornienko, G. A. Somorjai and P. Yang, *Nat. Mater.*, 2016, **15**, 1188–1194.
19 X. Wang, S.-I. Choi, L. T. Roling, M. Luo, C. Ma, L. Zhang, M. Chi, J. Liu, Z. Xie, J. A. Herron, M. Mavrikakis and Y. Xia, *Nat. Commun.*, 2015, **6**, 7594.
20 X. Huang, H. Zhang, C. Guo, Z. Zhou and N. Zheng, *Angew. Chem., Int. Ed.*, 2009, **48**, 4808–4812.
21 H. Zhang, M. Jin and Y. Xia, *Chem. Soc. Rev.*, 2012, **41**, 8035–8049.
22 L. Wang and Y. Yamauchi, *J. Am. Chem. Soc.*, 2013, **135**, 16762–16765.
23 S. Bai, C. Wang, W. Jiang, N. Du, J. Li, J. Du, R. Long, Z. Li and Y. Xiong, *Nano Res.*, 2015, **8**, 2789–2799.
24 Y.-X. Xiao, J. Ying, G. Tian, Y. Tao, H. Wei, S.-Y. Fan, Z.-H. Sun, W.-J. Zou, J. Hu, G.-G. Chang, W. Li, X.-Y. Yang and C. Janiak, *Appl. Catal., B*, 2019, **259**, 118080.
25 J. Ying, G. Jiang, Z. P. Cano, L. Han, X.-Y. Yang and Z. Chen, *Nano Energy*, 2017, **40**, 88–94.
26 K. Wang, H. Du, R. Sriphathoorat and P. K. Shen, *Adv. Mater.*, 2018, **30**, 1804074.
27 Y.-W. Lee, J.-Y. Lee, D.-H. Kwak, E.-T. Hwang, J. I. Sohn and K.-W. Park, *Appl. Catal., B*, 2015, **179**, 178–184.
28 P. Yang, X. Yuan, H. Hu, Y. Liu, H. Zheng, D. Yang, L. Chen, M. Cao, Y. Xu, Y. Min, Y. Li and Q. Zhang, *Adv. Funct. Mater.*, 2018, **28**, 1704774.
29 J. Xie, Q. Zhang, L. Gu, S. Xu, P. Wang, J. Liu, Y. Ding, Y. F. Yao, C. Nan, M. Zhao, Y. You and Z. Zou, *Nano Energy*, 2016, **21**, 2 47–257.